Characterization and physical modeling of MOS capacitors in epitaxial graphene monolayers and bilayers on 6H-SiC

Characterization and physical modeling of MOS capacitors in epitaxial graphene monolayers and bilayers on 6H-SiC

M. Winters, E. Ö. Sveinbjörnsson, C. Melios, O. Kazakova, W. Strupiński, and N. Rorsman

Citation: AIP Advances **6**, 085010 (2016); doi: 10.1063/1.4961361
View online: http://dx.doi.org/10.1063/1.4961361
View Table of Contents: http://scitation.aip.org/content/aip/journal/adva/6/8?ver=pdfcov
Published by the AIP Publishing

Characterization and physical modeling of MOS capacitors in epitaxial graphene monolayers and bilayers on 6H-SiC

M. Winters,[1,a] E. Ö. Sveinbjörnsson,[2,3] C. Melios,[4,5] O. Kazakova,[4] W. Strupiński,[6] and N. Rorsman[1]

[1]*Chalmers University of Technology, Dept. of Microtechnology and Nanoscience, Kemivägen 9, 412-96 Göteborg Sweden*
[2]*University of Iceland, Science Institute, IS-107 Reykjavik, Iceland*
[3]*Linköping University, Department of Physics, Chemistry and Biology (IFM), 58-183 Linköping, Sweden*
[4]*National Physical Laboratory, Teddington, TW11 0LW United Kingdom*
[5]*Advanced Technology Institute, University of Surrey, Guildford, Surrey, GU2 7XH, United Kingdom*
[6]*Institute of Electronic Materials Technology, Wóczyńska 133, 01-919 Warsaw, Poland*

(Received 8 February 2016; accepted 5 August 2016; published online 12 August 2016)

Capacitance voltage (CV) measurements are performed on planar MOS capacitors with an Al_2O_3 dielectric fabricated in hydrogen intercalated monolayer and bilayer graphene grown on 6H-SiC as a function of frequency and temperature. Quantitative models of the CV data are presented in conjunction with the measurements in order to facilitate a physical understanding of graphene MOS systems. An interface state density of order $2 \cdot 10^{12} \mathrm{eV}^{-1}\mathrm{cm}^{-2}$ is found in both material systems. Surface potential fluctuations of order 80-90meV are also assessed in the context of measured data. In bilayer material, a narrow bandgap of 260meV is observed consequent to the spontaneous polarization in the substrate. Supporting measurements of material anisotropy and temperature dependent hysteresis are also presented in the context of the CV data and provide valuable insight into measured and modeled data. The methods outlined in this work should be applicable to most graphene MOS systems. [http://dx.doi.org/10.1063/1.4961361]

I. INTRODUCTION

The electron transport properties of graphene monolayers and bilayers have generated significant amount of interest and competitive high speed field effect devices have been demonstrated in both materials.[1,2] Intercalated monolayers and bilayers grown by epitaxy on SiC are particularly promising as they routinely demonstrate the excellent transport properties and material uniformity required for the fabrication of microwave integrated circuits.[3,4] However, field effect devices in graphene often demonstrate poor current modulation which significantly compromises high frequency performance.[5–7] In metal-oxide-semiconductor (MOS) systems, current modulation is strongly affected by dielectric quality and charge trapping effects. As graphene is a gapless semiconductor, devices in graphene are expected to demonstrate subdued current modulation relative traditional semiconductor devices. For this reason, graphene devices are particularly sensitive to dielectric charging and interface trapping effects as they can easily screen current modulation. This trade-off between exceptional material properties and non-ideal dielectrics warrant an investigation of charge control in metal-oxide-graphene systems.

Capacitance-voltage (CV) and conductance-voltage (GV) measurements are commonly used to investigate interface states and trapping effects in MOS systems such as silicon, SiC,[8] and III/V

[a]Corresponding author email: micwinte@chalmers.se

heterostructures.[9] The CV/GV technique indirectly probes the interaction of charge carriers with other aspects of the MOS system such as interface states (D_{it}), surface potential fluctuations ($\delta\epsilon_f$), material non-uniformity, and substrate polarization (ΔP).

Charge control in graphene MOS systems has been investigated previously, and recent studies have sought to quantify the quantum capacitance (C_q) of monolayers and bilayers in top gated field effect devices.[10] Surface potential fluctuations ($\delta\epsilon_f$) were later addressed in the context of graphene monolayers and bilayers, and results were treated phenomenologically as a broadening of the density of states in graphene.[11] In exfoliated monolayers on SiO_2, Dröscher et al. attribute poor current modulation in top gated structures to surface potential fluctuations of order 100meV.[12] In Ref. 13, charge control is investigated in monolayers transferred onto SiO_2 with an Al_2O_3 gate dielectric grown by atomic layer deposition (ALD). Results demonstrate dispersion in the CV curves associated with interface states (D_{it}), and temperature dependence is attributed to thermally activated charge trapping in the dielectric.

It is also necessary to consider substrate induced effects in graphene MOS systems. In epitaxial graphene on 4H(6H)-SiC in particular, the spontaneous polarization of the substrate (ΔP) is responsible for the hole conductivity observed in intercalated monolayers and bilayers.[14] Additionally, ΔP is known to open a narrow energy gap (ϵ_g) in epitaxial bilayers, which has important consequences for interpreting CV data.[15,16]

In this work, a quantitative physical model of charge control in graphene monolayers and bilayers is presented in conjunction with temperature dependent CV/GV measurements performed on planar MOS capacitors.The devices are fabricated in hydrogen intercalated epitaxial monolayers and bilayers grown on 6H-SiC with a thin Al_2O_3 gate dielectric. The dielectric is prepared by repeated deposition and subsequent thermal oxidation of thin layers of Al metal, a technique which frequently appears in the literature as an alternative to atomic layer deposition (ALD).[17–19]

With accurate modeling, a number of relevant device parameters including the density of interface states, the magnitude of surface potential fluctuations, and the presence of a narrow energy gap in bilayers induced by the spontaneous polarization of the substrate are assessed in a single experiment. Supporting measurements addressing surface potential fluctuations, hysteresis, and charge injection are also discussed in order to facilitate a deeper understanding of the CV/GV data. While developed in the context of epitaxial graphene on SiC, a straightforward application of the modeling methods outlined in this work should be sufficient to describe CV/GV data in a wide variety of graphene MOS systems.

II. THEORY

An analysis of charge control in a MOS capacitor begins by considering the modulation of the Fermi energy ϵ_f by an applied voltage v. The total capacitive response observed in a CV measurement may be expressed as

$$\frac{1}{C_{tot}(\epsilon)} = \frac{1}{C_{ox}} + \frac{1}{e^2\rho(\epsilon) + e^2 D_{it}(\epsilon)} \tag{1}$$

In Eq. (1), C_{ox} represents the oxide capacitance, $C_q = e^2\rho(\epsilon)$ the quantum capacitance in graphene, and $C_{it} = e^2 D_{it}(\epsilon)$ the capacitance due to interface states.[20,21] Eq. (1) implies the following relation between ϵ_f and v[22]

$$\frac{1}{e}\frac{\partial\epsilon}{\partial v} = \frac{C_{ox}}{C_{ox} + e^2\rho(\epsilon) + e^2 D_{it}(\epsilon)} \tag{2}$$

Integrating equation Eq. (2) over $\epsilon \in [0, \epsilon_f]$ and $v \in [v_D, v]$ yields the following expression.

$$\Delta v - \frac{e^2}{C_{ox}}\int_{v_D}^{v} D_{it}(v)dv = \frac{\epsilon_f}{e} + \frac{e}{C_{ox}}n(\epsilon_f) \tag{3}$$

In Eq. (3), $\Delta v = v - v_D$ where v_D is the Dirac voltage ($\epsilon_f = 0$). Eq. (3) is the equivalent of the Berglund integral in graphene MOS.[23] The electron density may be calculated via the Fermi-Dirac

integral.

$$n_e(\epsilon_f) = \int_0^\infty \rho(\epsilon) f(\epsilon : \epsilon_f, k_b T) d\epsilon \tag{4}$$

In Eq. (4), k_b is Boltzmann's constant and T is the absolute temperature. The occupation statistics are given by the Fermi-Dirac distribution $f(\epsilon : \epsilon_f, k_b T) = [1 + e^{(\epsilon-\epsilon_f)/k_b T}]^{-1}$. The hole density $n_h(\epsilon_f)$ may be obtained by transforming $\epsilon_f \rightarrow -\epsilon_f$ and integrating over $\epsilon \in [0, -\infty)$. The total carrier density is then given by $n = n_e + n_h$. When $\epsilon_f \gg 0$ electron density dominates and when $\epsilon_f \ll 0$ hole density dominates. An ambipolar condition occurs near $\epsilon_f \approx 0$, as both electron and hole density contribute to the total carrier density. The monolayer and bilayer density of states relations are

$$\begin{aligned} \rho_m(\epsilon_f) &= \frac{g_s g_v}{2\pi} \frac{|\epsilon_f|}{(\hbar v_f)^2} \\ \rho_b(\epsilon_f) &= \frac{g_s g_v}{2\pi} \frac{|\epsilon_f| + \gamma_\perp/2}{(\hbar v_f)^2} \end{aligned} \tag{5}$$

where, $g_s(g_v)$ are the twofold spin(valley) degeneracies respectively, $v_f \approx 1 \cdot 10^8$cm/s is the Fermi velocity in graphene, and $\hbar$ is the reduced Plank constant. In the case of bilayer graphene, the density of states in Eq. (5) is approximated as the sum of the density of states at low and high energy. The quantity $\gamma_\perp \approx 0.4$ eV represents the interlayer coupling constant in Bernal stacked bilayers.[24]

In order to accurately model CV curves, it is necessary to account for interface states (D_{it}). Generally, the effect of a large D_{it} is to compromise charge control in the channel by screening C_q. A common approach to estimate D_{it} is to compare the capacitive response of the MOS structure at low and high frequency.[9]

$$eD_{it}^*(v) = \left(\frac{C_{ox} C_{tot}^0}{C_{ox} - C_{tot}^0} - \frac{C_{ox} C_{tot}^\infty}{C_{ox} - C_{tot}^\infty} \right) \tag{6}$$

When a MOS capacitor is biased at low frequency, the total capacitance C_{tot}^0 will contain contributions from C_{ox}, C_q, and C_{it}. As the frequency of the test signal is increased, interface states will contribute less to the total capacitance observed. In the case of very high frequencies only C_q and C_{ox} will contribute to the observed capacitance C_{tot}^∞. This dispersive effect in the C_{tot} is due to the finite capture and emission lifetimes ($\tau_{c,e}$) of trap states. In the majority of dielectric/semiconductor systems, $\tau_e \gg \tau_c$ such that the dominant contribution to frequency dependence in C_{tot} is τ_e.

Eq. (6) tends to underestimate D_{it} especially when $C_q \gg C_{it}$. In order to account for this, the effective D_{it} may be estimated by multiplying Eq. (6) by a scaling factor D_0. The dispersive effect due to the finite lifetimes of trap states is well described by a simple exponential where $\omega = 2\pi f$ is the angular frequency.

$$D_{it}(v, \omega) = D_0 D_{it}^*(v) e^{-\omega \tau_e} \tag{7}$$

The movement of charge in and out of interface states gives rise to a small signal conductance G_{it} such that D_{it} can be estimated by examining the frequency dependence of G_{it}.

$$\left(\frac{G_{it}}{\omega} \right) = \frac{e\omega\tau_e D_{it}}{1 + (\omega\tau_e)^2} \tag{8}$$

Eq. (8) exhibits a maximum in conductance when interface states are in resonance with the test signal.

When analyzing CV data, it is also necessary to account for surface potential fluctuations ($\delta\epsilon_f$). Surface potential fluctuations describe a spatial variation in ϵ_f due to charge inhomogeneities at the graphene/substrate and graphene/oxide interfaces. In graphene, surface potential fluctuations are especially relevant near $\epsilon_f = 0$ as they generate localized islands of electron and hole conduction.[25–27] In order to model surface potential fluctuations, it is useful to introduce a random variable to describe the Fermi energy $\tilde{\epsilon}_f$.

$$\tilde{\epsilon}_f = \mathcal{N}(\epsilon_f) \tag{9}$$

The distribution $\mathcal{N}$ represents the statistics which describe the spatial variations of ϵ_f. Typically, $\mathcal{N}$ may be assumed to be normally distributed.

$$\mathcal{N}(\epsilon : \epsilon_f, \delta\epsilon) = \exp\left(\frac{-(\epsilon - \epsilon_f)^2}{2(\delta\epsilon)^2}\right) \tag{10}$$

In Eq. (10) the terms ϵ_f and $\delta\epsilon$ represent the mean standard deviation of the Fermi energy statistics $\tilde{\epsilon}_f$.

$$\delta\epsilon = \delta\epsilon_f \exp\left(\frac{-\epsilon_f^2}{2(\delta\sigma_f)^2}\right) \tag{11}$$

$\delta\epsilon_f$ represents the root mean square (RMS) value of surface potential fluctuations near the Dirac point. Eqs. (10) and (11) describe a case where the magnitude of the surface potential fluctuations decays with standard deviation $\delta\sigma_f$ as one moves further from $\epsilon_f = 0$. Generally the term $\delta\sigma_f$ is found to be of order 100meV such that $\delta\epsilon \approx \delta\epsilon_f$ near the Dirac point. When $|\epsilon_f| \gg 0$, surface potential fluctuations have little effect on the behavior of the CV characteristic.

In this work, we propose the following method to model CV-curves in graphene. First, D_{it}^* may be estimated via Eq. (6). As this is known to be an underestimation, the scale parameter D_0 is then introduced and the corresponding D_{it} may be included. If a negative D_0 is required to obtain accurate high frequency capacitance curves, then the measurement data must be corrected for inductance. Typically, an inductance correction is only needed for measurement frequencies exceeding 1MHz. Using $D_{it}(v,\omega)$, one may obtain $\epsilon_f(v,\omega)$ via Eq. (3) via nonlinear optimization methods. In order to obtain proper capacitance curves, it is necessary to account for surface potential fluctuations. This is accomplished via a kind of Monte Carlo simulation in which noisy $\epsilon_f(v,\omega)$ curves are generated via Eqs. (10) and (11). These are then used to calculate noisy capacitance curves via Eq. (1). Results are then averaged in order to obtain a final model.

III. METHODS

CV(GV) measurements are performed as a function of temperature on 10000μm^2 planar MOS capacitors using an Agilent E4980A LCR meter. The geometry of the MOS capacitors is shown in Fig. 1. In the CV measurements, the applied bias is swept quasistatically from -2 to 2V, and the capacitive(conductive) responses of the device to a 10mV test signal are measured at several

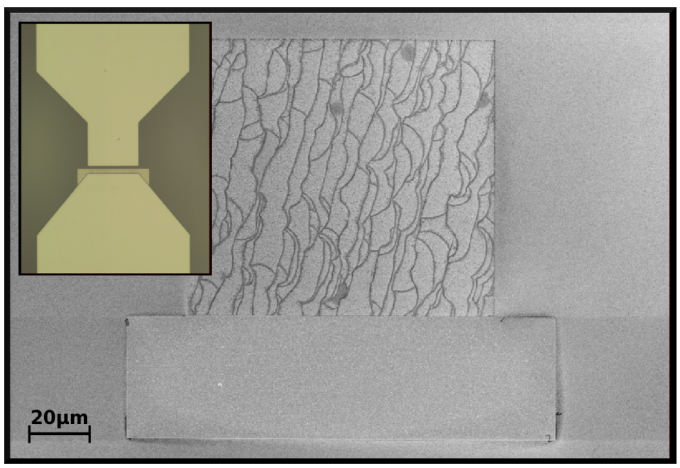

FIG. 1. A scanning electron microscopy image of a 10 000 μm^2 etched mesa in monolayer graphene prior to the deposition of aluminium oxide. Bilayer coverage is observed on terrace edges, and occasional bilayer inclusions are seen on terrace. [inset] An optical image showing the design of a completed planar MOS device.

frequencies $f \in [1, 10, 100, 200, 500, 1000\text{kHz}]$. All measurements consist of a forward and reverse sweep in order to track hysteretic effects in the devices.

The monolayer and bilayer samples were grown on semi-insulating (SI) 6H-SiC by chemical vapour deposition (CVD) and in-situ intercalated with hydrogen.[28,29] Upon intercalation, both monolayers and bilayers exhibit hole conduction ($\epsilon_f < 0$) as a consequence of the spontaneous polarization of the substrate.[14] Prior to device fabrication, the samples were characterized via microwave reflectivity measurements and scanning electron microscopy (SEM) in order to assess material quality and the number of layers. The microwave reflectivity measurements yielded mobilities of 4500(3000)$\text{cm}^2/\text{V}\cdot s$ and carrier densities of $0.95(0.87)\cdot 10^{13}\text{cm}^{-2}$ for the monolayer(bilayer) samples.

Dielectric deposition on graphene is challenging owing to the fact that low temperature processes are required. For this reason, high-κ dielectrics such as Al_2O_3 are often deposited on graphene via atomic layer deposition (ALD). However, several studies document the difficulty of achieving uniform layers with ALD as the Al_2 $(CH_3)_6$ precursor does not effectively wet pristine graphene.[30] To circumvent this, a nucleation layer is often used (2-3nm) in order to facilitate the growth of the subsequent ALD layer.[31,32] The nucleation layer is usually thermally oxidized aluminium (as is shown in our study), though polymer functionalization has also been shown to be effective. When thin dielectric layers are needed, thermally oxidized aluminium is usually sufficient with regard to leakage thus precluding the need for the subsequent ALD step.

The Al_2O_3 dielectric was deposited by repeated evaporation and subsequent hotplate oxidation at 200°C of 1nm aluminium metal films. In both samples, a target oxide thickness (t_{ox}) of 15nm was chosen in order to ensure adequate coverage of the terraced morphology of the SiC substrate. The thermal oxidation method was chosen in part because the resulting oxide demonstrated excellent leakage characteristics on the large area MOS devices (<1nS at 1kHz). Similar tests on nucleated 15nm ALD layers demonstrated nonuniform coverage on terrace edges along with considerable leakage (>1μS at 1kHz) such that a reliable extraction of D_{it} via the CV method was not feasible. However, as the interface is identical in both systems, there should little difference between the two methods with regard to (D_{it}) provided a high quality ALD layer with uniform coverage is achieved.

In addition to the planar MOS devices, ancillary van der Pauw (vdP) structures and Transfer Length Method (TLM) structures are included to assess the low field transport properties and contact resistance after processing. From these structures, mean mobilities of 1601(2028) $\text{cm}^2/\text{V}\cdot s$ and carrier densities of $1.05(0.79)\cdot 10^{13}\text{cm}^{-2}$ are obtained for the monolayer(bilayer) samples. Measurements on the TLM structures indicated a contact resistance of $300(200)\Omega\cdot\mu m$ for the monolayer(bilayer) samples.

The temperature sweep is carried out in a liquid N_2 cryostat, and the temperature is swept linearly from 77K to 280K. Additional measurements are performed at room temperature in order to investigate charge injection effects in connection with the hysteresis observed in the devices. In all CV curves presented in this work, a low frequency conductance of <1nS is observed.

In order to assess material uniformity, work function (ϕ_g), and surface potential fluctuations ($\delta\epsilon_f$) in epitaxial graphene, frequency modulated Kelvin Probe Force Microscopy (KPFM) is performed on small $25\mu\text{m}^2$ van der Pauw (vdP) structures.[33] As KPFM is only sensitive to the surface of a material, it was necessary to fabricate samples without the gate oxide present. Prior to performing KPFM, AFM cleaning was performed in contact mode to remove contaminants and residues from the surface. As graphene is sensitive to atmospheric and polymer contaminants, it is necessary to perform the KPFM measurements in a controlled atmosphere.[34–36] Prior to scanning, the chamber was evacuated and then subsequently filled with N_2 at room temperature. Finally, the atmosphere was saturated to a relative humidity of 30% to approximate ambient conditions. The work function calibration was done using $\phi_g = \phi_{probe} - eV_{cpd}$ where V_{cpd} is the measured surface potential. The probe work function (ϕ_{probe}) was calibrated against the an Au contact electrode within the scan area.

Modeling the CV curves is computationally difficult as a combination of Monte Carlo methods, nonlinear methods, and parameter optimization is required. For this reason, an efficient CV simulation kernel was implemented on a graphics processor (GPU). GPU processing offers the flexibility of a massively parallel computation scheme in a highly threaded environment allowing for efficient Monte Carlo simulations [supplementary material].

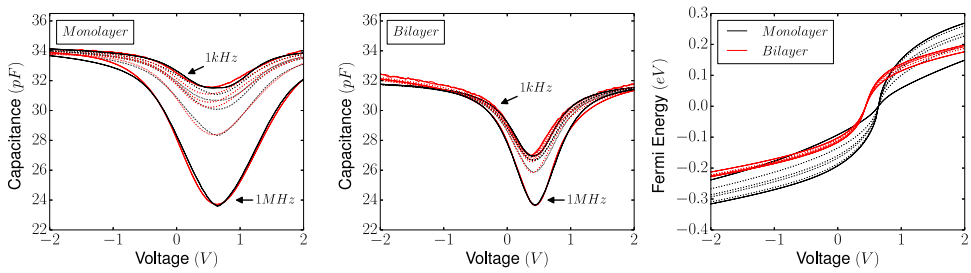

FIG. 2. Measured (red) and modeled (black) CV curves for monolayer [left] and bilayer [centre] graphene MOS capacitors. The capacitance is measured as a function at several frequencies from 1 kHz to 1MHz. The low frequency and high frequency curves are shown solid, while intermediate frequencies are shown dotted. Note the dispersive effect whereby the capacitance minimum in C_{tot} reduces with increasing frequency. [right] The extracted $\epsilon_f(v)$ curves corresponding to the modeled monolayer and bilayer capacitance curves. The measurements are performed at 77K.

IV. CV CHARACTERISTICS IN GRAPHENE MOS CAPACITORS

The measured and modeled low frequency CV characteristics at 77K are shown in Fig. 2 for both monolayer and bilayer material. $\epsilon_f(v_g)$ as calculated from Eq. (3) is also shown. Both materials exhibit a minimum in capacitance which corresponds to $\epsilon_f = 0$. As both materials are intercalated, $v_D > 0$ indicating hole density at zero bias. Moving away from v_D in either direction, the capacitance increases and then saturates indicating accumulation of carriers at the graphene/oxide interface. In the saturation regions, $C_q \gg C_{ox}$ such that the oxide capacitance and dielectric constant may be estimated $\kappa = C_{ox}t_{ox}/\varepsilon_0$. Additionally, the CV curves are approximately symmetric around v_D, which reflects the symmetric behavior of $\rho_{m,b}(\epsilon_f)$ around $\epsilon_f = 0$ (see Eq. (5)).

All parameters for the modeled monolayer and bilayer capacitance curves of Fig. 2 are shown in Table I. In the following sections, details are presented with respect to the implementation and interpretation of modeling results. First, a commentary on D_{it} is provided. Next, surface potential fluctuations and material non-uniformity are addressed in the context of SEM and KPFM imaging. Energy gap modeling in bilayers then described, and a band diagram for the graphene MOS systems is proposed. Finally, charge injection and hysteresis are discussed alongside temperature dependent measurements.

A. Characterization of Interface States

Both monolayer and bilayer material exhibit significant dispersion when measuring CV(GV) curves as a function of frequency. By fitting the CV(GV) measurement data to Eqs. (7) and (8), independent estimates of D_{it} and τ_e may be made. The estimation of τ_e and D_{it} via the 77K CV data of Fig. 2 is shown in Fig. 3.

A D_{it} of $3.75(1.51)\cdot10^{12}\text{eV}^{-1}\text{cm}^{-2}$ is extracted from the monolayer(bilayer) material from the CV curves via Eq. (7). Similar values of $1.51(1.50)\cdot10^{12}\text{eV}^{-1}\text{cm}^{-2}$ are obtained from modeling GV curves via Eq. (8). This should be compared with a D_{it} of 10^{12}-$10^{13}\text{eV}^{-1}\text{cm}^{-2}$ reported for 30nm ALD layers prepared on CVD graphene transferred to SiO_2/p-Si substrates.[37] Similar values of $10^{12}\text{eV}^{-1}\text{cm}^{-2}$ have been reported in AlGaN/GaN heterostructures with low temperature ALD Al_2O_3 gate dielectrics.[38] For comparison, values as low as $5\times10^{10}\text{eV}^{-1}\text{cm}^{-2}$ and $10^{11}\text{eV}^{-1}\text{cm}^{-2}$

TABLE I. A table summarizing the model parameters for the 77K CV curves shown in Fig. 2. The density of interface states (D_{it}) is reported in units of $10^{12}\text{eV}^{-1}\text{cm}^{-2}$ for $\epsilon_f = 0$, and parentheses represent extractions from CV(GV) curves respectively. Note that the ϵ_g and σ_g values in monolayer material apply only to its 20% bilayer component. The quantities are grouped according to their relevant effect.

	C_{ox} (pF)	κ	$v_D(V)$	D_0	D_{it}	$\tau_e(\mu s)$	$\delta\epsilon_f$(meV)	$\delta\sigma_f$(meV)	ϵ_g(meV)	σ_g(meV)	p(%ML)
Monolayer	35.6	5.76	0.6	8.0	3.75(1.75)	0.82(0.55)	91	156	274*	92*	0.8
Bilayer	33.0	5.42	0.4	6.9	1.51(1.50)	0.34(0.38)	78	105	260	80	0.1

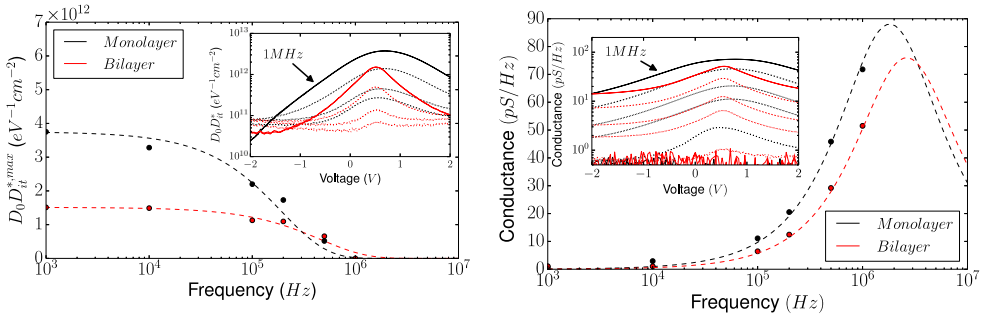

FIG. 3. [left] The extraction of the τ_e via the exponential decay of $D_0D_{it}^*$ with increasing frequency (Eq. (7)). [inset] The estimated $D_0D_{it}^*$ as calculated from the difference of high frequency and low frequency capacitances. [right] The estimation of τ_e from Eq. (8). [inset] The GV curves measured corresponding to the CV curves shown in Fig. 2. The 1MHz curves are shown solid, while lower frequencies are shown dotted. Data for monolayer(bilayer) material is shown in black(red) respectively.

have been achieved in silicon and SiC MOS devices respectively with high temperature SiO_2 dielectrics.[39,40]

From Fig. 2, the monolayer material exhibits the larger swing in Fermi energy with $\epsilon_f \in [-0.32, 0.28\text{eV}]$ over the applied bias range. Thus, the measurement only probes an energy interval at the dielectric/graphene interface over 0.60eV near the middle of the dielectric band gap. The D_{it} for such a limited energy range are in most cases rather flat (e.g for SiO_2 and Al_2O_3 on SiC and Si) such that the peak in D_{it} near v_D is an artifact of the extraction. When v is far from v_D, C_q is large such that a estimation of D_{it} by Eq. (7) is difficult. For this reason, the maximum density of interface states D_{it}^{max} occurring at $\epsilon_f = 0$ is taken to estimate the true D_{it}.

B. Surface Potential Fluctuations & Material Uniformity

The effect of surface potential fluctuations is to generate a distributed capacitance minimum in the CV characteristics. In the case of a monolayer, $C_q(\epsilon_f) \to 0$ when $\epsilon_f = 0$ such that C_{tot}^{∞} should sharply approach zero near v_D. The fact that such a minimum is not seen in measurement data demonstrates the effect of surface potential fluctuations ($\delta\epsilon_f$). Modeling the CV characteristics in monolayers and bilayers yields values of 92(78)meV for $\delta\epsilon_f$. This should be compared with values of 100meV, 25-40meV and 30-100meV in graphene, Si, and SiC MOS devices respectively.[12,41,42]

The results of KPFM imaging are shown in Fig. 4. The magnitude of the surface potential fluctuations in pristine graphene may be compared with those extracted from CV measurements. The work function data is normally distributed for the monolayer(bilayer) regions with mean of $\phi_g \approx 4.82(4.73)$eV. Equating the surface potential fluctuations as the work function RMS for the entire active area, one has $\delta\epsilon_f \approx \delta\phi_g \approx 80$ meV in relative agreement with what is obtained from CV modeling. The KPFM data indicates that monolayer(bilayer) inclusions contribute significantly to magnitude of surface potential fluctuations.

The SEM and KPFM images of Figs. 1 and 4 show that the large area monolayer MOS capacitors have bilayer inclusions which have an effect on the CV characteristics. These inclusions are a consequence of the growth mechanism. During epitaxy, graphene growth nucleates at step edges and propagates over the terrace. On monolayer(bilayer) samples, bilayer(multilayer) graphene is common on terrace edges respectively.[43] Additionally, inclusions of monolayer(bilayer) material in bilayer(monolayer) samples may also appear on terraces.[44]

It is straightforward to account for inclusions in CV modeling by considering the density of states as linear combination of the monolayer and bilayer relations (Eq. (5)).

$$\rho_{eff}(\epsilon) = p\rho_m(\epsilon) + (1-p)\rho_b(\epsilon) \tag{12}$$

In Eq. (12), the quantity p represents the mixing ratio of monolayer area to the total area of the device. In order to estimate p, SEM imaging was performed on monolayer and bilayer material. Terraces and terrace edges are clearly visible on the surface of the substrate. In Fig. 1, low

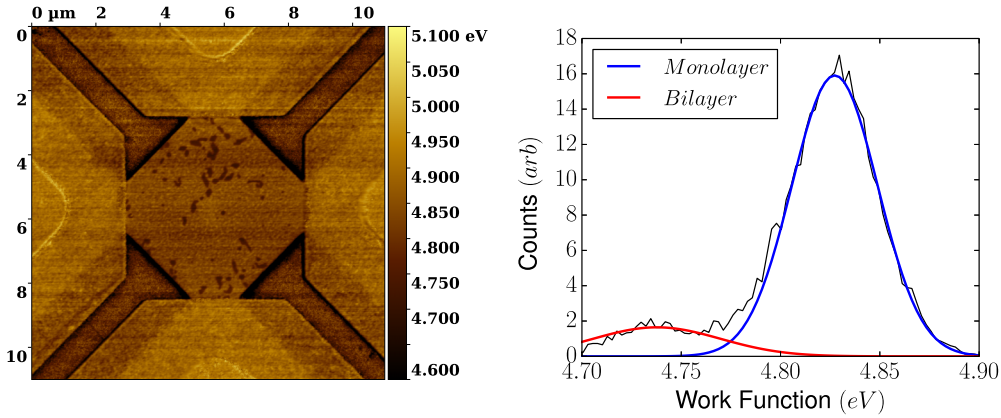

FIG. 4. [left] KPFM(work function) measurements on a 25µm^2 van der Pauw structure. The active area of the device is completely on terrace, and inclusions of bilayer material are clearly visible as regions of lower work function. [right] A histogram of the work function observed active area of the image. The statistics of work function fluctuations for monolayer(bilayer) regions are well described by a normal distributions blue(red).

contrast regions correspond to monolayer material while high contrast regions correspond to bilayer material. Values of 0.8(0.1) were obtained from imaging monolayer(bilayer) material respectively.

C. Graphene MOS Band Diagrams

The energy band diagram for the graphene MOS system as shown in Fig. 5 provides a useful context to understand CV measurements. The mean work function of ϕ_g = 4.8 eV for graphene estimated from the KPFM measurements is in relative agreement with literature values.[36,45,46] The estimation of the ϕ_g from KPFM is calibrated relative to the work function of the Au contact metalization.

As the amount of mobile charge in the semi-insulating SiC is negligible, there should be minimal band bending in the SiC bulk. Thus, ϵ_f passes through the midgap such that the band offset between the conduction band in the SiC and the ϵ_f in the graphene is $\epsilon_g^{SiC}/2$. The band gap in 6H-SiC is $\epsilon_g^{SiC} \approx 3.0$ eV resulting in a band offset of 1.5 eV.[14,47]

The band gap in Al_2O_3 oxide ϵ_g^{ox} has been shown vary with the phase of the material and its quality. Values for high quality crystaline films range from 8.8 eV in α-Al_2O_3 to 7.1-8.0 eV in γ-Al_2O_3. For lower quality amorphous films, values of 5.1-7.1 eV are reported.[48,49] Measurements

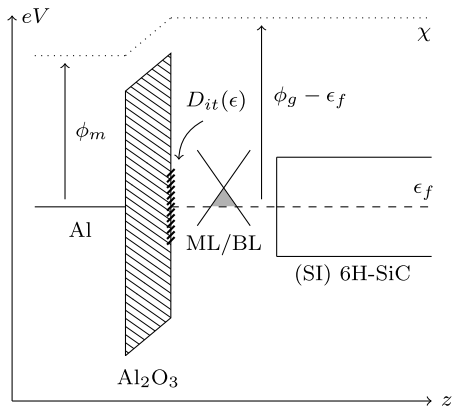

FIG. 5. A band diagram of the graphene MOS system with several important quantities indicated. The graphene monolayer/bilayer component of the system is represented schematically via the Dirac cone. The Fermi energy ϵ_f is referenced relative to the Dirac point, and energy values are shown approximately to scale.

for the conduction band offset between in the amorphous Al_2O_3/SiC system yield values of 2.06 eV such that the charge neutrality point in the graphene lies near the midgap in the Al_2O_3.[50–52] For this reason, Al_2O_3 is an ideal dielectric for graphene MOS on SiC.

D. Energy Gaps in Bilayer MOS

Although the CV characteristic observed in monolayers and bilayers is qualitatively similar, the physical origin of the capacitance minimum is different. This may be seen by returning to the expression for the total capacitance (Eq. (1)). At high frequency, $C_{it} \approx 0$ such that the total capacitance is simply $C_{tot} = [C_q^{-1} + C_{ox}^{-1}]^{-1}$. In both monolayer and bilayer material, a minimum in C_{tot} is expected at $\epsilon_f = 0$. However, in a bilayer $C_q \neq 0$ when $\epsilon_f = 0$. Evaluating the theoretical quantum capacitance in a bilayer, a value of 4.170 μF/cm^2 is obtained at $\epsilon_f = 0$. For the $A = 10000\mu m^2$ bilayer capacitors $C_q A = 471$ pF. As the observed oxide capacitance is $C_{ox}A \approx 33$ pF, the minimum expected capacitance at high frequency in the bilayer MOS pads is $C_{tot}^{min}A \approx 30.8$ pF.

The minimum high frequency capacitance observed in the bilayer data (23.2pF) is significantly lower than the expected 30.8pF (see Fig. 2). In order to account for the anomalous behavior, it is necessary to introduce an energy gap ϵ_g into the density of states relation near $\epsilon_f = 0$.

$$\rho_b(\epsilon) = \rho_b^0(\epsilon)\rho_g(\epsilon : \epsilon_g, \sigma_g) \tag{13}$$

The notion of an energy gap in graphene bilayers is well understood, and results in a symmetry breaking of the bilayer Hamiltonian which occurs when the individual layers are at different potential energies.[15,16] In bilayer MOS, there are two sources of such potential which function to open a gap: the high density of interface states at the graphene/oxide interface D_{it}, and the spontaneous polarization of the 6H-SiC substrate ΔP. In both cases the sheet charge density involved is of order 10^{12}cm^{-2} at minimum, such that a symmetry breaking of the bilayer Hamiltonian is realistic. The notion of an energy gap is additionally supported by the fact that the 1 kHz CV curve in bilayer material exhibits a significantly deeper capacitance minimum than the monolayer case despite comparable D_{it} and $\delta\epsilon_f$.

The presence of surface potential fluctuations (80-90meV) reflects that the charge densities involved are not uniform. In this case, the magnitude of the energy gap will vary locally from point to point within the bilayer MOS structure such that an empirical model is needed for $\rho_g(\epsilon : \epsilon_g, \sigma_g)$.

$$\rho_g(\epsilon : \epsilon_g, \sigma_g) = 1 - \frac{1}{2}\mathrm{erfc}\left(\frac{\epsilon + \epsilon_g/2}{\sqrt{2}\sigma_g}\right) + \frac{1}{2}\mathrm{erfc}\left(\frac{\epsilon - \epsilon_g/2}{\sqrt{2}\sigma_g}\right) \tag{14}$$

The effect of Eq. (14) is to cut a smoothed notch out of the bilayer density of states relation in (Eq. (5)). Here ϵ_g represents the mean value of the energy gap, while σ_g characterizes its dispersion. Results from CV modeling suggest an energy gap of 260meV in the case of the bilayer sample, and a value of 274meV for the bilayer component of the monolayer sample. These values are in qualitative agreement with experiments in dual gated field effect transistors, in which a narrow energy gap of $\epsilon_g = 250$ meV has been observed.[53,54] Polarization induced gaps of order $\epsilon_g = 150$ meV have also been observed epitaxial bilayers on SiC.[55]

V. DISCUSSION

The quantitative nature of the CV model becomes evident when considering sensitivity with regard to the parameters of Table I. A particular sensitivity is observed with respect to $\delta\epsilon_f$ and ϵ_g as summarized in Fig. 6. Further, all parameters introduced into the model are physical with the possible exception of $\delta\sigma_f$. In the Si and SiC cases, the magnitude of the surface potential fluctuations is typically independent of bias such that $\delta\sigma_f \to \infty$. In the context of the CV model, $\delta\sigma_f$ effectively corrects for the artificial profile of D_{it} obtained from Eq. (6). The strong low frequency dispersion near the Dirac point in the monolayer and bilayer samples presented in this work suggests that the electron traps are physically located at the graphene/oxide interface or within the

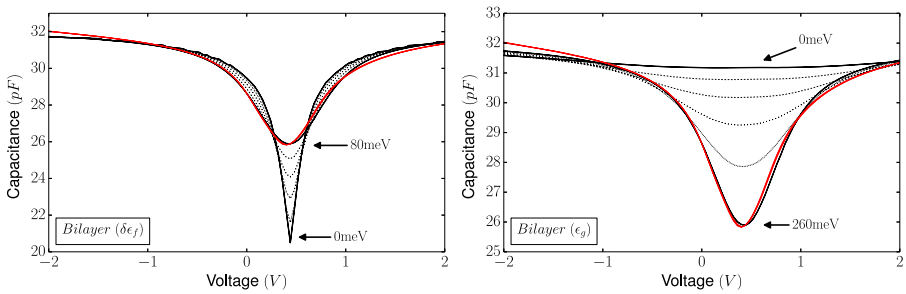

FIG. 6. [left] A demonstration of the sensitivity of modeled 1MHz CV curves on surface potential fluctuations for bilayer material. $\delta\epsilon_f$ is scaled linearly from 0meV to the 80meV arrived at by modeling. [right] A similar demonstration regarding ϵ_g sensitivity in bilayers. In both plots the measured CV curve is shown in red while modeled curves are shown in black.

graphene sheet itself. Physically, vacancies in native Al_2O_3 dielectric located at the graphene/oxide interface and inclusions in the graphene likely account for the observed dispersion.

The dispersion observed in this work is in contrast to what is observed in transferred layers on SiO_2 in which the low frequency dispersion is observed under accumulation.[13] In the devices investigated by Lin et al., dispersion is observed under accumulation suggesting that trapping occurs above the graphene/oxide interface (i.e. in the dielectric itself). To account for this behavior, the authors suggest two trap bands for their ALD oxides which are spaced somewhat symmetrically around $\epsilon_f = 0$. This is different than our case, in which the dispersion suggests one continuous trap band of approximately constant D_{it}. Thus, the interpretation of dispersive characteristics highlights important differences between in interface trapping mechanisms between native Al_2O_3 and ALD Al_2O_3 dielectrics on graphene.

When measuring the CV characteristic as a function of temperature, several additional effects are observed which are not considered in the CV model (Fig. 7). First, a hysteresis of anti-clockwise orientation opens in both samples for temperatures(thermal energies) greater than 160K(13.7meV). Hysteresis is a common problem in the context of graphene field effect transistors and has been attributed to a plurality of mechanisms.[56–58] The orientation of the hysteresis is significant and suggests a charge injection effect.[59,60]

By comparing the extracted forward (v_D^f) and reverse (v_D^r) sweep Dirac points a similar trend appears in both materials. Generally, v_D^f is constant, while v_D^r increases suggesting that charge injection occurs only when $\epsilon_f > 0$. Electron conduction in amorphous Al_2O_3 layers is supported by current-voltage measurements in p-Si MOS structures with an ALD Al_2O_3 dielectric.[61] In Ref. 61, Novikov et al. show a strong temperature dependence in the leakage current through their ALD Al_2O_3 layers above 77K. In order to account for electron conduction a multiphonon ionization mechanism for deep levels is described.[62] A bulk trap density(activation energy) of $2 \cdot 10^{20}$ cm^{-3} (1.5 eV) is estimated from the multiphonon ionization model. The high density of deep levels is relevant as it implies temperature dependent transport through the amorphous Al_2O_3 layer via the

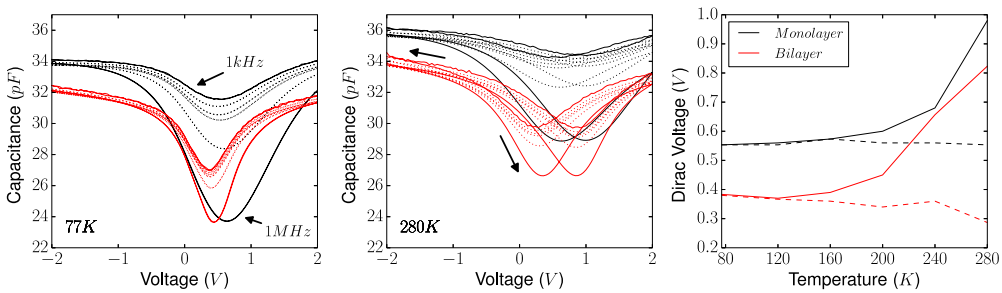

FIG. 7. [left/centre] The CV curves for monolayer(bilayer) MOS capacitors at 77K and 280K. Monolayer curves are shown in black, while bilayer curves are shown in red. A hysteresis in the CV characteristic opens in both materials around $160K$ suggesting a thermally activated trapping effect. Arrows for the 280K bilayer curves indicate the anti-clockwise orientation of the hysteresis. [right] v_D plotted as a function of temperature for the forward(dashed) and reverse(solid) sweeps.

ionization of deep levels. Transport is determined to be monopolar(electron), and the temperature dependence described is qualitatively consistent with that of the hysteresis observed in the CV measurements presented in this work. For this reason, it is reasonable to suggest that deep levels in the oxide are responsible for hysteresis shown in Fig. 7.

In monolayer(bilayer) a $v_D^r - v_D^f$ of 0.43(0.52V) is observed at 280K indicating similar levels of charge injection in both materials. Repeated CV sweeps of increasing amplitude reveal a drift of the capacitance minima towards positive bias indicating permanent injection of negative charge into the oxide layer. In addition to hysteresis, a monotonic increase in the zero bias capacitance is observed with increasing temperature. In Ref. 13, similar trends are also attributed to a thermally activated trap mechanism. The effect of oxide charging is deleterious with regard to effective charge control as the lagging of ϵ_f behind v generates a more shallow slope and additional broadening of the CV characteristic on either side of v_D. The charge injection hysteresis is observed at all frequencies owing to the fact that it is a DC effect. The frequency relevant to charge injection is the sweep rate of the applied bias rather that of the test signal.

The effectiveness of charge control can be estimated by considering the ratio of the carrier density in accumulation n^{acc} to the intrinsic carrier density. From modeling CV data, the maximal ϵ_f is approximately -320(-220)meV for monolayer(bilayer) material. This corresponds to a carrier density of approximately $0.78(1.03)\cdot 10^{13}\text{cm}^{-2}$. The intrinsic (i.e. $\epsilon_f = 0$) electron densities are given by the following relations.[63]

$$\begin{aligned} n_e^m(0) &= \frac{\pi}{6}\frac{(k_bT)^2}{(\hbar v_f)^2} \\ n_e^b(0) &= n_m(0) + \frac{\log(2)}{\pi}\frac{\gamma_\perp k_bT}{(\hbar v_f)^2} \end{aligned} \tag{15}$$

Counting both electrons and holes, the above relations evaluate to $0.16(2.79)\cdot 10^{12}\text{cm}^{-2}$ at 77K. This suggests a ratio $n^{acc}/n^{tot}(0)$ of 469(36) in monolayer(bilayer) material suggesting that charge control should be much more effective in the monolayers. However, in the presence of surface potential fluctuations, the RMS carrier densities become $0.51(2.86)\cdot 10^{12}\text{cm}^{-2}$ such that a reduced ratio of 15(3.6) is expected at 77K. Modulation of the carrier density in both cases is further limited by the presence of $D_{it} \approx 2\cdot 10^{12}$ $\text{eV}^{-1}\text{cm}^{-2}$. In the case of monolayer material, D_{it} destroys the remaining modulation of carrier density at low frequency. In bilayer material, some charge control is preserved due to $\epsilon_g \approx 260$meV.

VI. CONCLUSIONS

A method to model measured CV data in graphene MOS structures has been described. With accurate models, it is possible to estimate the density of interface states D_{it}, the magnitude of surface potential fluctuations $\delta\epsilon_f$, the effect of material anisotropy, and the presence of a narrow energy gap ϵ_g in bilayer material. The density of interface states is significant in both materials, and values of order $2\cdot 10^{12}$ $\text{eV}^{-1}\text{cm}^{-2}$ are extracted from measurement data. An analysis of the D_{it} results yields an emission lifetime τ_e of several hundred nanoseconds for the trap states. In both materials, surface potential fluctuations of order 80-90meV are found to generate a distributed capacitance minimum. Similar values are obtained from KPFM measurements, and surface potential fluctuations are found to be correlated with inclusions of monolayer(bilayer) material. An narrow energy gap of order 260meV is obtained for the bilayer constituents of both materials consequent to the spontaneous polarization of the substrate. An anti-clockwise hysteresis effect is observed due to a thermally activated trap in the dielectric. The hysteresis is found to be temperature dependent, and a thermal barrier of about 160K(13.7meV) is deduced from temperature dependent CV data. The hysteresis has a deleterious effect on charge control, and generates considerable broadening in the CV characteristics of both MOS systems.

These results are of interest from a physical and technological perspective as they suggest a need to improve dielectric quality and material uniformity in graphene MOS devices. The effect of D_{it} and $\delta\epsilon_f$ substantially compromise charge control in graphene MOS systems. Monolayer

material exhibits poor charge control characteristics as a direct consequence of these effects. In bilayers, some degree of charge control is maintained due to the opening of a narrow energy gap indicating that bilayers may be more applicable in a transistor context.

SUPPLEMENTARY MATERIAL

See supplementary material for a GPU implementation of the GMOS CV model (2016).

ACKNOWLEDGEMENT

This work was supported by the European Science Foundation (ESF) under the EUROCORES Program EuroGRAPHENE, and by the EU Graphene Flagship (No. 604391). We also acknowledge support from the Swedish Foundation for Strategic Research (SSF), and the Knut and Alice Wallenberg Foundation (KAW).

[1] J. A. Robinson, M. Hollander, I. Michael LaBella, K. A. Trumbull, R. Cavalero, and D. W. Snyder, Nano Letters **11**, 3875 (2011), pMID: 21805993, http://dx.doi.org/10.1021/nl2019855, URL http://dx.doi.org/10.1021/nl2019855.
[2] B.N. Szafranek, G. Fiori, D. Schall, D. Neumaier, and H. Kurz, Nano Letters **12**, 1324 (2012), pMID: 22339809, http://dx.doi.org/10.1021/nl2038634, URL http://dx.doi.org/10.1021/nl2038634.
[3] J. A. Robinson, M. Hollander, M. LaBella, K. A. Trumbull, R. Cavalero, and D. W. Snyder, Nano Letters **11**, 3875 (2011), http://pubs.acs.org/doi/pdf/10.1021/nl2019855, URL http://pubs.acs.org/doi/abs/10.1021/nl2019855.
[4] M. Winters, O. Habibpour, I. Ivanov, J. Hassan, E. Janzén, H. Zirath, and N. Rorsman, Carbon **81**, 96 (2015), ISSN 0008-6223, URL http://www.sciencedirect.com/science/article/pii/S0008622314008811.
[5] H. Xu, Y. Chen, J. Zhang, and H. Zhang, Small **8**, 2833 (2012), ISSN 1613-6829, URL http://dx.doi.org/10.1002/smll.201102468.
[6] H. Wang, A. Hsu, D. S. Lee, K. K. Kim, J. Kong, and T. Palacios, Electron Device Letters, IEEE **33**, 324 (2012), ISSN 0741-3106.
[7] M. Winters, E. Ö. Sveinbjörnsson, and N. Rorsman, Journal of Applied Physics **117**, 074501 (2015), URL http://scitation.aip.org/content/aip/journal/jap/117/7/10.1063/1.4913209.
[8] G. Chung, C. Tin, J. Williams, K. McDonald, R. Chanana, R. Weller, S. Pantelides, L. C. Feldman, O. Holland, M. Das *et al.*, Electron Device Letters, IEEE **22**, 176 (2001).
[9] R. Engel-Herbert, Y. Hwang, and S. Stemmer, Journal of Applied Physics **108**, 124101 (2010), URL http://scitation.aip.org/content/aip/journal/jap/108/12/10.1063/1.3520431.
[10] J. Xia, F. Chen, J. Li, and N. Tao, Nature nanotechnology **4**, 505 (2009).
[11] G. Kliros, in *Semiconductor Conference (CAS), 2010 International* (2010), Vol. 01, pp. 69–72 ISSN 1545-827X.
[12] S. Dröscher, P. Roulleau, F. Molitor, P. Studerus, C. Stampfer, K. Ensslin, and T. Ihn, Applied Physics Letters **96**, 152104 (2010), URL http://scitation.aip.org/content/aip/journal/apl/96/15/10.1063/1.3391670.
[13] H. Lin, I. Asselberghs, A. Vais, G. Arutchelvan, A. Delabie, M. Heyns, A. Mocuta, I. Radu, and A. Thean, Microelectronic Engineering **147**, 314 (2015), ISSN 0167-9317, insulating Films on Semiconductors 2015, URL http://www.sciencedirect.com/science/article/pii/S0167931715003512.
[14] J. Ristein, S. Mammadov, and T. Seyller, Phys. Rev. Lett. **108**, 246104 (2012), URL http://link.aps.org/doi/10.1103/PhysRevLett.108.246104.
[15] T. Ohta, A. Bostwick, T. Seyller, K. Horn, and E. Rotenberg, Science **313**, 951 (2006), URL http://www.sciencemag.org/content/313/5789/951.abstract.
[16] T. Ohta, A. Bostwick, J. L. McChesney, T. Seyller, K. Horn, and E. Rotenberg, Phys. Rev. Lett. **98**, 206802 (2007), URL http://link.aps.org/doi/10.1103/PhysRevLett.98.206802.
[17] Z. Feng, C. Yu, J. Li, Q. Liu, Z. He, X. Song, J. Wang, and S. Cai, Carbon **75**, 249 (2014), ISSN 0008-6223, URL http://www.sciencedirect.com/science/article/pii/S0008622314003170.
[18] A. Badmaev, Y. Che, Z. Li, C. Wang, and C. Zhou, ACS Nano **6**, 3371 (2012), pMID: 22404336, http://dx.doi.org/10.1021/nn300393c, URL http://dx.doi.org/10.1021/nn300393c.
[19] E. Guerriero, L. Polloni, L. G. Rizzi, M. Bianchi, G. Mondello, and R. Sordan, Small **8**, 357 (2012), ISSN 1613-6829, URL http://dx.doi.org/10.1002/smll.201102141.
[20] S. Dröscher, P. Roulleau, F. Molitor, P. Studerus, C. Stampfer, K. Ensslin, and T. Ihn, Physica Scripta **2012**, 014009 (2012), URL http://stacks.iop.org/1402-4896/2012/i=T146/a=014009.
[21] G. Zebrev, E. Melnik, and D. Batmanova, in *Microelectronics (MIEL), 2012 28th International Conference on* (2012), pp. 335–338.
[22] A. Penumatcha, S. Swandono, and J. Cooper, Electron Devices, IEEE Transactions on **60**, 923 (2013), ISSN 0018-9383.
[23] C. Berglund, Electron Devices, IEEE Transactions on 701–705 (1966).
[24] S. Das Sarma, S. Adam, E. H. Hwang, and E. Rossi, Rev. Mod. Phys. **83**, 407 (2011), URL http://link.aps.org/doi/10.1103/RevModPhys.83.407.
[25] J. Martin, N. Akerman, G. Ulbricht, T. Lohmann, J. Smet, K. Von Klitzing, and A. Yacoby, Nature Physics **4**, 144 (2008).
[26] Z. Yuanbo *et al.*, Nature Letters **459**, 820 (2009), URL http://www.nature.com/nature/journal/v459/n7248/full/nature08105.html.

[27] M. Gibertini, A. Tomadin, F. Guinea, M. I. Katsnelson, and M. Polini, Phys. Rev. B **85**, 201405 (2012), URL http://link.aps.org/doi/10.1103/PhysRevB.85.201405.
[28] C. Riedl, C. Coletti, T. Iwasaki, A. A. Zakharov, and U. Starke, Phys. Rev. Lett. **103**, 246804 (2009), URL http://link.aps.org/doi/10.1103/PhysRevLett.103.246804.
[29] W. Strupinski, K. Grodecki, A. Wysmolek, R. Stepniewski, T. Szkopek, P. E. Gaskell, A. Gruneis, D. Haberer, R. Bozek, J. Krupka *et al.*, Nano Letters **11**, 1786 (2011), http://pubs.acs.org/doi/pdf/10.1021/nl200390e, URL http://pubs.acs.org/doi/abs/10.1021/nl200390e.
[30] X. Wang, S. M. Tabakman, and H. Dai, Journal of the American Chemical Society **130**, 8152 (2008), pMID: 18529002, http://dx.doi.org/10.1021/ja8023059, URL http://dx.doi.org/10.1021/ja8023059.
[31] S. Kim, J. Nah, I. Jo, D. Shahrjerdi, L. Colombo, Z. Yao, E. Tutuc, and S. K. Banerjee, Applied Physics Letters **94**, 062107 (2009), URL http://scitation.aip.org/content/aip/journal/apl/94/6/10.1063/1.3077021.
[32] P. Ye, A. Neal, T. Shen, J. Gu, M. Bolen, and M. Capano, ECS Transactions **33**, 459 (2010).
[33] V. Panchal, R. Pearce, R. Yakimova, A. Tzalenchuk, and O. Kazakova, Scientific reports **3** (2013).
[34] T. Burnett, R. Yakimova, and O. Kazakova, Nano Letters **11**, 2324 (2011), pMID: 21526826, http://dx.doi.org/10.1021/nl200581g, URL http://dx.doi.org/10.1021/nl200581g.
[35] Y.-J. Yu, Y. Zhao, S. Ryu, L. E. Brus, K. S. Kim, and P. Kim, Nano Letters **9**, 3430 (2009), pMID: 19719145, http://dx.doi.org/10.1021/nl901572a, URL http://dx.doi.org/10.1021/nl901572a.
[36] D. Ziegler, P. Gava, J. Güttinger, F. Molitor, L. Wirtz, M. Lazzeri, A. M. Saitta, A. Stemmer, F. Mauri, and C. Stampfer, Phys. Rev. B **83**, 235434 (2011).
[37] U. Jung, Y. J. Kim, Y. Kim, Y. G. Lee, and B. H. Lee, IEEE Electron Device Letters **36**, 408 (2015), ISSN 0741-3106.
[38] C. Mizue, Y. Hori, M. Miczek, and T. Hashizume, Japanese Journal of Applied Physics **50**, 021001 (2011), URL http://stacks.iop.org/1347-4065/50/i=2R/a=021001.
[39] R. R. Razouk and B. E. Deal, Journal of The Electrochemical Society **126**, 1573 (1979).
[40] K. Fukuda, S. Suzuki, T. Tanaka, and K. Arai, Applied Physics Letters **76** (2000).
[41] G. Declerck, R. Van Overstraeten, and G. Broux, Journal of Applied Physics **45** (1974).
[42] E. Bano, T. Ouisse, L. Di Cioccio, and S. Karmann, Applied Physics Letters **65** (1994).
[43] J. Hassan, M. Winters, I. Ivanov, O. Habibpour, H. Zirath, N. Rorsman, and E. Janzén, Carbon **82**, 12 (2015), ISSN 0008-6223, URL http://www.sciencedirect.com/science/article/pii/S0008622314009725.
[44] I. G. Ivanov, J. U. Hassan, T. Iakimov, A. A. Zakharov, R. Yakimova, and E. Janzén, Carbon (2014), ISSN 0008-6223, URL http://www.sciencedirect.com/science/article/pii/S0008622314005065.
[45] J. K. Park, S. M. Song, J. H. Mun, and B. J. Cho, Nano Letters **11**, 5383 (2011), pMID: 22059809, http://dx.doi.org/10.1021/nl202983x, URL http://dx.doi.org/10.1021/nl202983x.
[46] S. M. Song, J. K. Park, O. J. Sul, and B. J. Cho, Nano Letters **12**, 3887 (2012), pMID: 22775270, http://dx.doi.org/10.1021/nl300266p, URL http://dx.doi.org/10.1021/nl300266p.
[47] M. E. Levinshtein, S. L. Rumyantsev, and M. S. Shur, *Properties of Advanced Semiconductor Materials: GaN, AlN, InN, BN, SiC, SiGe* (John Wiley & Sons, 2001).
[48] R. H. French, Journal of the American Ceramic Society **73**, 477 (1990).
[49] B. Ealet, M. Elyakhloufi, E. Gillet, and M. Ricci, Thin Solid Films **250**, 92 (1994), ISSN 0040-6090, URL http://www.sciencedirect.com/science/article/pii/0040609094901716.
[50] S. Toyoda, T. Shinohara, H. Kumigashira, M. Oshima, and Y. Kato, Applied Physics Letters **101**, 231607 (2012), URL http://scitation.aip.org/content/aip/journal/apl/101/23/10.1063/1.4769818.
[51] E. O. Filatova and A. S. Konashuk, The Journal of Physical Chemistry C **119**, 20755 (2015), http://dx.doi.org/10.1021/acs.jpcc.5b06843, URL http://dx.doi.org/10.1021/acs.jpcc.5b06843.
[52] C. M. Tanner, Y.-C. Perng, C. Frewin, S. E. Saddow, and J. P. Chang, Applied Physics Letters **91**, 203510 (2007), URL http://scitation.aip.org/content/aip/journal/apl/91/20/10.1063/1.2805742.
[53] E. V. Castro, K. S. Novoselov, S. V. Morozov, N. M. R. Peres, J. M. B. L. dos Santos, J. Nilsson, F. Guinea, A. K. Geim, and A. H. C. Neto, Phys. Rev. Lett. **99**, 216802 (2007), URL http://link.aps.org/doi/10.1103/PhysRevLett.99.216802.
[54] Y. Zhang, T.-T. Tang, C. Girit, Z. Hao, M. C. Martin, A. Zettl, M. F. Crommie, Y. R. Shen, and F. Wang, Nature **459**, 820 (2009).
[55] S. Zhou, G.-H. Gweon, A. Fedorov, P. First, W. De Heer, D.-H. Lee, F. Guinea, A. C. Neto, and A. Lanzara, Nature materials **6**, 770 (2007).
[56] T. Lohmann, K. von Klitzing, and J. H. Smet, Nano Letters **9**, 1973 (2009).
[57] H. Wang, Y. Wu, C. Cong, J. Shang, and T. Yu, ACS Nano **4**, 7221 (2010), pMID: 21047068.
[58] B. H. Lee, Y. G. Lee, U. J. Jung, Y. H. Kim, H. J. Hwang, J. J. Kim, and C. G. Kang, Carbon Letters 23–28 (2012).
[59] M. Egginger, S. Bauer, R. Schwödiauer, H. Neugebauer, and N. Sariciftci, Monatshefte für Chemie - Chemical Monthly **140**, 735 (2009), ISSN 0026-9247, URL http://dx.doi.org/10.1007/s00706-009-0149-z.
[60] A. M. Burke, D. E. J. Waddington, D. J. Carrad, R. W. Lyttleton, H. H. Tan, P. J. Reece, O. Klochan, A. R. Hamilton, A. Rai, D. Reuter *et al.*, Phys. Rev. B **86**, 165309 (2012), URL http://link.aps.org/doi/10.1103/PhysRevB.86.165309.
[61] Y. N. Novikov, V. A. Gritsenko, and K. A. Nasyrov, Applied Physics Letters **94**, 222904 (2009), URL http://scitation.aip.org/content/aip/journal/apl/94/22/10.1063/1.3151861.
[62] S. Makram-Ebeid and M. Lannoo, Phys. Rev. B **25**, 6406 (1982), URL http://link.aps.org/doi/10.1103/PhysRevB.25.6406.
[63] J. Ristein, W. Zhang, F. Speck, M. Ostler, L. Ley, and T. Seyller, Journal of Physics D: Applied Physics **43**, 345303 (2010), URL http://stacks.iop.org/0022-3727/43/i=34/a=345303.